

The Arches cluster out to its tidal radius: dynamical mass segregation and the effect of the extinction law on the stellar mass function. [★]

M. Habibi^{1,3}, A. Stolte¹, W. Brandner², B. Hußmann¹, K. Motohara⁴

¹ Argelander Institut für Astronomie, Universität Bonn, Auf dem Hügel 71, 53121 Bonn, Germany e-mail: [mhabibi;astolte;hussmann]@astro.uni-bonn.de

² Max-Planck-Institut für Astronomie, Königsstuhl 17, 69117 Heidelberg, Germany e-mail: brandner@mpia.de

³ Member of the International Max Planck Research School (IMPRS) for Astronomy and Astrophysics at the Universities of Bonn and Cologne.

⁴ Institute of Astronomy, The University of Tokyo, Osawa 2-21-1, Mitaka, Tokyo 181-0015, Japan e-mail: kmotohara@ioa.s.u-tokyo.ac.jp

Received Oct 14, 2012; accepted November 30, 2012

ABSTRACT

The Galactic Center is the most active site of star formation in the Milky Way Galaxy, where particularly high-mass stars have formed very recently and are still forming today. However, since we are looking at the Galactic Center through the galactic disk, knowledge of extinction is crucial to study the region. The Arches cluster is a young, massive starburst cluster, near the Galactic Center. We observed the Arches cluster out to its tidal radius using K_s band imaging obtained with NAOS/CONICA at the VLT combined with Subaru/Cisco J -band data to gain a full understanding of the cluster mass distribution. We show that the determination of the mass of the most massive star in the Arches cluster, which had been used in previous studies to establish an upper-mass limit for the star formation process in the Milky Way, strongly depends on the assumed slope of the extinction law. Assuming the two regimes of widely used infrared extinction laws we show that the difference can reach up to 30% in extracted initial mass and ~ 1 magnitude in acquired K_s -band extinction while the present mass function slope changes by ~ 0.17 dex. The present-day mass function slopes derived assuming the Nishiyama et al. (2009) extinction law are increasing from a flat slope of $\alpha_{Nishi} = -1.76 \pm 0.22$ in the core ($r < 0.2$ pc) to $\alpha_{Nishi} = -2.23 \pm 0.27$ in the intermediate annulus $0.2 < r < 0.4$ and become high mass depleted, $\alpha_{Nishi} = -2.95 \pm 0.26$, in the outer annulus ($0.4 < r < 1.5$ pc). This picture is consistent with mass segregation due to the dynamical evolution of the cluster.

Key words. Galaxy: center, open clusters and associations—: individual: Arches cluster, stellar dynamics, extinction map, — stars: mass function, luminosity function — stars: early-type — infrared: stars — instrumentation: adaptive optics

1. Introduction

The center of our galaxy hosts many massive molecular clouds, active sites of massive star formation, and a remarkable number of high-mass stars (Yusef-Zadeh et al. 2009). It contains three of the most massive and young star clusters in our Galaxy, namely: the Arches, Quintuplet and Young Central Cluster. The Arches cluster is the youngest among the three (~ 2.5 Myr, Najarro et al. 2004; Martins et al. 2008) which is located at a projected distance of ~ 25 pc from the Galactic Center (GC). This cluster contains many massive stars including 160 O-stars and 13 WN stars (Figer 2004; Martins et al. 2008). Providing a collection of high-mass stars and a very dense core ($\rho_{core} \sim 10^5 M_{\odot}/pc^3$; Espinoza et al. 2009) makes the Arches cluster an excellent site to address questions about massive star formation, the stellar mass function and the dynamical evolution of young, massive clusters in the GC.

However, the high extinction toward this cluster causes this investigation to be challenging. A visual extinction of up to 30

magnitudes allows the GC to be accessed only in the radio, infrared and X-ray regime. The extinction is due to the diffuse interstellar medium (Lebofsky 1979) as well as dense molecular clouds in the Central Molecular Zone (Morris & Serabyn 1996). The latter are suggested to contribute one-third of the total extinction (Williams et al. 2000). The substructure of molecular clouds (e.g. Williams et al. 2000) causes patchy extinction along the GC line of sight. The interstellar environment around the Arches cluster itself is also extreme. The Arches cluster is observable in the near infrared thanks to shedding its natal cloud but it is still surrounded by the molecular clouds with which the cluster is interacting (e.g. Yusef-Zadeh et al. 2002; Lang 2004).

The interstellar extinction toward the GC was first investigated by Rieke & Lebofsky (1985) by studying the color excess of five supergiants near the GC and the star σ Sco in the upper scorpius region. The extinction derived by Rieke & Lebofsky (1985) was later fitted to a power law $\propto \lambda^{-1.61}$ (Cardelli 1989) and considered in many studies as the standard extinction law toward the GC. Later studies analyzed: nebular hydrogen lines (eg. Lutz et al. 1996), near-infrared surveys (Nishiyama et al. 2009; Stead & Hoare 2009) and photometry of red clump stars in the GC (Schoedel et al. 2010), and revealed that the near-infrared extinction law in the range of the J , H and K_s bands is better described by a steeper power law with an index of $\alpha \sim -2.0$. The

[★] Based on observations collected at the ESO/VLT under Program ID 71.C-0344(A) (PI: F. Eisenhauer, retrieved from the ESO archive) and Program ID 081.D-0572(B) (PI: W. Brandner). Also based on data collected at the Subaru Telescope, which is operated by the National Astronomical Observatory of Japan.

slope of the extinction law influences the derivation of individual masses from the luminosities of cluster members, and hence has severe impacts on the stellar mass function as well as the upper mass limit derived from comparison with stellar evolution models.

Previous studies of the Arches cluster have been aware of the high extinction toward this cluster but chosen different methods to tackle the problem; therefore it is not surprising that different studies resulted in deviating present-day mass functions in the center of the Arches cluster. Figer et al. (1999) adopted a single extinction value of $A_K = 3.0$ mag and found a flat mass function for the Arches cluster compared to the standard Salpeter (1955) initial mass function. This finding opened a series of debates and further studies with the aim to distinguish between primordial or dynamical mass segregation. Stolte et al. (2002) and (2005) utilized deep adaptive optics (AO) observations to derive the present-day mass function within the cluster's half-mass radius. They treated the variable extinction of the cluster by correcting for a radial reddening gradient based on the extinction law of Rieke & Lebofsky (1985). A study by Kim et al. (2006) applied the extinction law of Rieke, Rieke & Paul (1989) and chose to correct for a single, mean extinction value for each of the observed cluster annuli and each control field. These studies confirmed the flattening of the mass function in the center of the cluster and also achieved to study the less massive sources in the cluster. Finally, Espinoza et al. (2009) used the general Galactic extinction law by Fitzpatrick (2004) to derive the present-day mass function. They acquired extinction parameters for the NACO/VLT natural photometric system and corrected the individual extinction toward each star.

In this paper we study the effects of the new regime of steeper near-infrared extinction laws on the derivation of individual stellar parameters toward the Arches cluster. K_s and H -band AO images taken with VLT/NACO as well as J -band images obtained with Subaru/CISCO are analyzed to cover the outskirts of the Arches cluster for the first time. This paper is organized as follows: in Sect. 2 we describe the data and observational setting. The data reduction steps, photometry and calibration processes are explained in Sect. 3. We determine the individual extinction values and construct the extinction map of the cluster in Sect. 4. In the last sub-section of Sect. 4 the individual stellar parameters derived assuming the two regimes of extinction laws are compared. We investigate the effect of the assumed slope of the extinction law on the determination of the mass of the most massive star in the Arches cluster, which had been used in previous studies to establish a upper-mass limit for the star formation process in the Milky Way. In Sect. 5, the present-day mass function of the Arches is constructed for an area which reaches to the tidal radius of the cluster for the first time. We probe the radial variation in the slope of the mass function in order to distinguish between primordial or dynamical mass segregation in the Arches cluster. A summary of our findings is presented in Sect. 6.

2. Observations

K_s band images ($\lambda_c = 2.18\mu\text{m}$, $\Delta\lambda = 0.35\mu\text{m}$) of the outer parts of the Arches cluster have been obtained on June 6-10 2008 with the Very Large Telescope (VLT). Images have been acquired with the near-infrared camera CONICA (Lenzen et al. 2003). The atmospheric turbulence was corrected with the AO system NAOS to enhance the spatial resolution (Rousset et al. 2003). We used the brightest star in K_s in each field as the natural guide source for the infrared wave-front sensor. Since the available natural guide stars are with $9.2 < K_s < 10.4$ mag at the faint limit

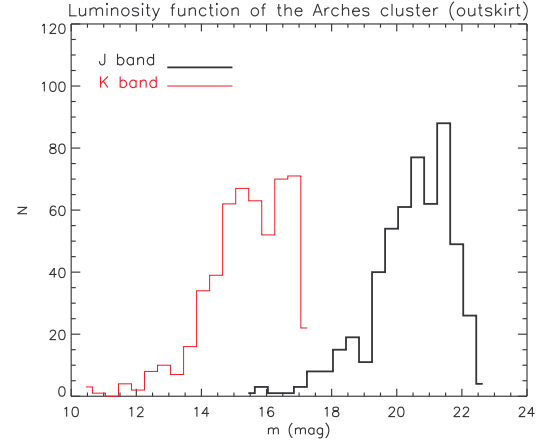


Fig. 1. The luminosity function is illustrated for the detected sources in the outskirts of the cluster in J -band and K_s -band images. The luminosity at which the number of stars decreases represents the detection limit of 21.5 mag and 17 mag for J -band and K_s -band observations respectively.

of the infrared wave-front sensor magnitude range, we had to use the N90C10 dichroic, which distributes 90% of the light to NAOS while only 10% are delivered to the science detector. We used Fowler sampling to enhance the sensitivity which allowed us to detect sources as faint as 17 mag (Fig. 1). The acquired images cover four fields of $27.8'' \times 27.8''$ each, provided by the medium resolution camera (S27) with a pixel scale of $0.027''$. On each of the 4 fields we obtained 44 dithered images with a detector integration time of 15 s and 2 exposures (NDIT=2), yielding 30 s of total exposure time per frame. We will refer to the four outer fields as fields 2-5. Small dither shifts with a maximum of $2''$ allowed a good background subtraction using the science frames while at the same time the optical distortions at the edges were minimized. During the K_s band observations the natural visual seeing varied from 0.61 to 0.98 (see Table 1). We achieved typical spatial resolutions of 3-4 pixels ($0.081'' - 0.135''$) on individual frames using this AO setup. The properties of all fields are summarized in Table 1.

We used the observations conducted in March 2002 on the central part of the Arches cluster using NAOS-CONICA in order to cover the whole cluster area. A visual guide star with $V=16.2$ mag was used for the visual wave-front sensor in the center. The data properties and reduction steps are described in Stolte et al. (2005) (see also Stolte (2003) for details). In this paper we will label this dataset as field 1.

Seeing-limited J -band ($\lambda_c = 1.25\mu\text{m}$, $\Delta\lambda = 0.16\mu\text{m}$) observations were performed on July 17th, 2000, with the 8.2 meter Subaru optical-infrared Telescope on Hawai'i (Iye et al. 2004) under excellent weather conditions. The CISCO spectrograph and camera (Motohara et al. 2002) provided a pixel scale of $0.116''$ and a field of view of $2' \times 2'$. We obtained 86 dithered J -band images with 10 s exposure time per image. An average seeing of $0.49''$ resulted into a Full Width at Half Maximum (FWHM) of the point-spread function (PSF) of $0.39''$ on the combined image (Table 1). The locations of the NACO fields overlaid on the SUBARU J -band image are shown in Fig. 2. The luminosity functions (Fig. 1) illustrate that the detection limits on the combined images are $K_s < 17$ and $J < 21.5$.

We also used the Galactic Plane Survey (GPS) of the UKIRT Infrared Deep Sky Survey (UKIDSS) (Lawrence et al. 2007) for calibration purposes. The UKIDSS survey started in 2005 using

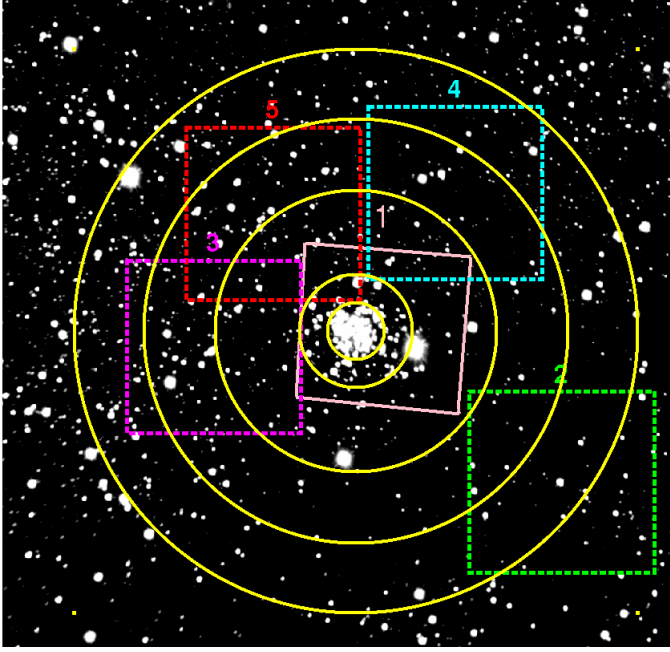


Fig. 2. The locations of the NACO fields (K_s -band observation) overlaid on the SUBARU J -band image of the Arches cluster. Circles illustrate distances of 0.2, 0.4, 1, 1.5 and 2 pc from the center of the cluster. The central field (field 1) is taken in K_s and H -band. North is up and East is to the left.

the wide field camera on the United Kingdom Infrared Telescope on Mauna Kea, Hawai'i. The GPS covered an area of 1800 square degrees in JHK to a depth of $K=19$ mag and $J=20$ mag. This survey is re-sampled to a uniform spatial resolution of $1''$, which is a factor of 2 improved compared to 2MASS. UKIDSS also probes 3 magnitudes deeper than 2MASS, such that it provides more accurate zero-pointing especially in crowded cluster fields (Lucas et al. 2008).

3. Data reduction

We have used a self-developed data reduction pipeline to reduce the NACO data. The body of this pipeline has been written in Python and it invokes some IRAF¹ tasks (Tody 1993) as well as custom-made IDL codes and Python routines. Images were dark subtracted with appropriate dark frames for each exposure time and flat fielded using twilight flats. A master dark frame was co-added using 3 individual dark frames to reduce the noise. To obtain the master flat, a robust linear fit was performed for each pixel on the detector to derive the pixel response at different flux levels. Bad pixels were revealed as pixels whose response after normalizing is less than 0.5 or more than 2. These bad pixels combined with hot and dead pixels detected during the combination of dark frames were written into a bad pixel mask. Ten off-cluster sky frames per field were taken at the end of each one hour observing block. A master sky was created using the IRAF task `imcombine` from only sky frames in the case of fields 2 and 5 while we acquired the smoothest master sky frame for fields 3 and 4 by combining both science and sky frames. Since it is not possible to find sky regions devoid of stars in the crowded

¹ IRAF is distributed by the National Optical Astronomy Observatory, which is operated by the Association of Universities for Research in Astronomy (AURA) under cooperative agreement with the National Science Foundation.

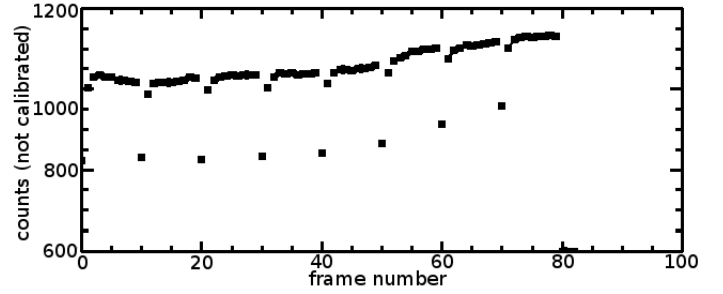


Fig. 3. The background level of individual frames taken with Subaru/Cisco is plotted in counts. After each shift of the telescope a discontinuity of $\sim 66\%$ was present in the background level of the frames. By scaling images to their background level the trend was taken out.

area of the GC, the number of $n_{\text{high}} = \text{number of sky frames} - 5$ brightest pixels were rejected to remove the residual star light from the master sky. We used the IRAF task `cosmicray` to reject individual pixels with fluxes 8 times above the background standard deviation as cosmic-rays in each individual science frame. We added each cosmic-ray mask to the bad pixel mask to obtain individual masks for each science frame.

Before co-adding the reduced images we calculated the FWHM of a reference source in each field. Combining images with low FWHM provides a higher resolution in the final image while adding a fewer number of images might cause a loss in sensitivity. In order to avoid degradation of the spatial resolution in the combined images we selected images with a FWHM of less than $0.0813'' - 0.1355''$ depending on the quality in each field. The number of combined images for each field are listed in Table 1. The acquired FWHM values were used to weight the individual images during image combination so that images with low FWHM gained higher weights.

We combined the weighted science images using the IRAF task `drizzle` (Fruchter & Hook 2002). Drizzle implies the individual bad pixel mask to discard hot pixels and other image defects during image combination.

The CISCO data were reduced within IRAF and employing some custom-made IDL routines. Comparing the background level of different frames revealed the obvious trend of discontinuity present in the background (Fig. 3). The trend was the result of moving and re-setting the telescope to capture dithered images so that in the first three images after each shift the background level was down to 66% ². We divided the data according to their background levels into four groups and scaled each group to the mean count of the background level. Scaled images were flat-fielded with twilight flats. Images for sky subtraction and bad pixel masks were created in the same way as for the NACO data. In order to prepare images for cross-correlation, we applied the IRAF task `precor` on all science images. Using `precor` we removed the majority of cosmic-rays and hot pixels by calculating the fraction of pixels in a 3×3 pixel box which had a value above a specified threshold. The task `crossdriz` was then run on the cleaned images to create a set of cross-correlation frames. Then the shifts between images were determined using the cross-correlation frames and images were combined with the drizzle algorithm (Fruchter et al. 2002) using a bad pixel mask created earlier.

² This instrumental issue is known as "reset anomaly" and is well known for many HAWAII arrays (see e.g. <http://www.ast.cam.ac.uk/~optics/cirsi/documents/resetanomaly.html>).

Table 1. Overview of the observations.

Field	Date	Filter	DIT \times NDIT (s) ^(a)	N_{frames}	N_{use}	Airmass	Seeing ^(b) (")	FWHM of PSF (")
<i>VLT/NACO</i>								
field 1 (center)	2002-03-30	H	30.00×2	35	14	1.15	0.8	0.084
field 1 (center)	2002-03-30	K_s	15.00×4	15	7	1.15	0.8	0.084
field 2 (outskirt)	2008-06-06	K_s	15.00×3	44	38	1.01	0.61–0.78	0.073
field 3 (outskirt)	2008-06-06	K_s	15.00×3	44	32	1.06	0.69–0.92	0.089
field 4 (outskirt)	2008-06-06	K_s	15.00×3	44	33	1.14	0.78–0.98	0.079
field 5 (outskirt)	2008-06-10	K_s	15.00×3	44	30	1.01	0.7–0.84	0.116
<i>Subaru/Cisco</i>								
wide field	2000-07-17	J	10.00×1	86	72	1.72	–	0.39

Notes. ^(a) Integration time for each exposure \times number of exposures. ^(b) Optical (V-band) seeing.

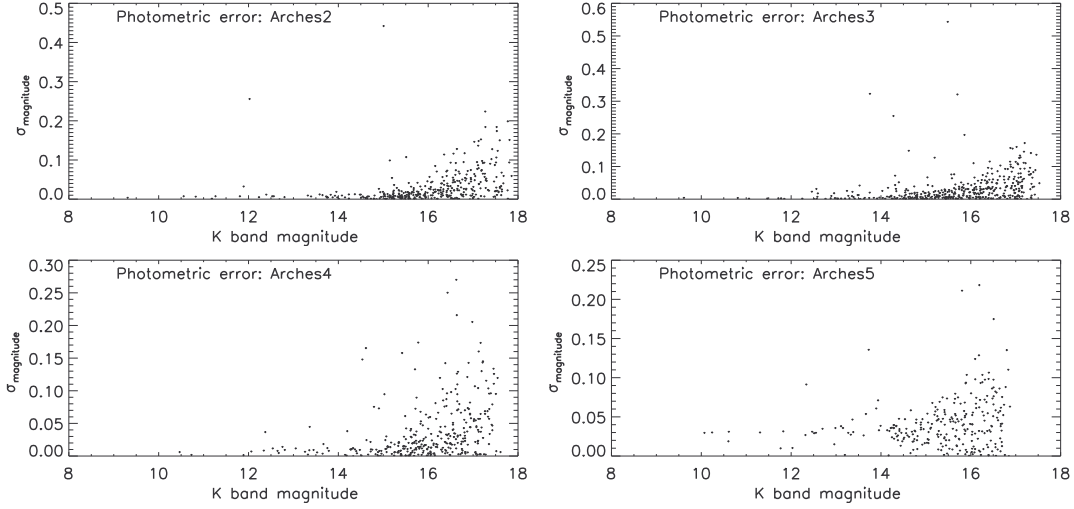


Fig. 4. Standard deviation of the individual K_s -band magnitudes in the 3 auxiliary frames, $\sigma_{magnitude}$, is plotted over the magnitude. As we expect the brighter sources have smaller photometric error. The value of $\sigma_{magnitude}$ for the majority of the sources is less than 0.2 mag.

3.1. Photometry

The photometry was extracted using Starfinder, an IDL PSF fitting package specifically developed to analyze AO data (Diolaiti et al. 2000). Starfinder’s PSF fitting algorithm extracts the empirical PSF from an image by a median combination of suitable stars. For this reason we used 10–15 reference stars in each field, chosen to be relatively isolated, bright and equally distributed over the field. However, since it is not easy to find such stars in crowded fields, secondary sources close to selected stars were first removed. A circular mask of 80 pixel diameter was used as the PSF size. Starfinder performs a cross-correlation check to determine the similarity of potential stars with the PSF. For the source extraction we set the correlation threshold to ≥ 0.7 to accept sources as potential stars. The final PSF was extracted after two cleaning iterations and three iterations were performed to detect stars with a count level of 3σ above the average background in the image.

Starfinder assumes a constant PSF across the image which is not exactly the case in wide-field AO imaging. The fact that AO performance is highly dependent on the distance from the guide star, anisoplanatism, can lead to a spatial trend in the amplitude and shape of the photometric residual in the PSF subtracted frames. We used 10–15 stars in each field to extract the average PSF for PSF fitting. To account for the residual flux variation the ratio of the flux in the PSF fitting residual to the stellar

flux was plotted against position. We detected a systematic linear trend with position, which could affect our photometry by 0.2 mag in fields 2, 3 and 5. We corrected the stellar fluxes, F_{star} , by fitting a linear function, $C_{fit}(x)$ to the flux ratio, $\frac{F_{res}}{F_{star}}$:

$$F_{corr,star}(i) = F_{star}(i) + (C_{fit}(x) \times F_{star}(i)) \quad (1)$$

where x is the position of the i th star. This flux correction allows a uniform zeropoint correction to be applied across each field (see Sect. 3.2).

In order to measure the photometric errors, we created three sub-lists of images for each field, each containing an equal number of images in a way that images with similar qualities (strehl-ratio) are distributed equally in the lists. The three lists were drizzled into three auxiliary frames for each field. We then applied the same Starfinder source extraction as in the deep science images. We estimated the photometric error of each star by measuring the standard deviation of the independent magnitude measurements in the three auxiliary images (Fig. 4). The value of $\sigma_{magnitude}$ for the majority of the sources is less than 0.1 mag.

3.2. Calibration

Since there are no red standard stars available, we use local standards in our fields for zeropoint calibration. The similarity of the VLT/NACO and UKIDSS filter systems allows us to use calibrated sources in the UKIDSS catalogue as zeropoint

sources (Lawrence et al. 2007). The UKIDSS photometry in turn was calibrated using numerous numbers of sources in the Two Micron All Sky Survey (2MASS). The photometric transformations between UKIDSS and 2MASS are given in Lucas et al. (2008) for the GPS.

The FWHM of the empirical PSF extracted from NACO images is $0.079 - 0.116''$ while the UKIDSS survey uses an aperture size of $1''$ to extract stellar fluxes. The high spatial resolution of NACO allows us to resolve many stars which are not resolved in the UKIDSS catalog but contribute to the measured aperture fluxes. In order to compare star fluxes on the same basis, we added up the fluxes from objects on our NACO frames within a radius of r_a as follows: $r_a = \text{UKIDSS aperture} - \text{one stellar radius} = 1'' - (0.5 \times \text{FWHM}_{\text{PSF}})$ where FWHM_{PSF} is the FWHM of the PSF for each NACO image.

The calibration is done independently for each field of the VLT/NACO 2008 data. We pick 10-15 stars in each field as possible reference sources. A sigma clipping is performed to avoid a residual bias from unresolved multiples or variable stars. The remaining 7-8 stars are used as the most consistent calibration reference stars to derive the zeropoint. The same procedure is performed to calibrate the J -band CISCO data as well as the 2002 VLT/NACO data taken in the central part of the Arches cluster. Since the aperture size of UKIDSS is only 2 times the FWHM of the extracted PSF of the CISCO image (0.49 arcsec) there is no need to add J -band fluxes to improve the calibration.

As shown in Fig. 2, some fields are overlapping with each other. Since the calibration of each field is done independently we use stars lying in these overlap regions to check the photometric calibration. Field 1 was in excellent agreement with field 4 and field 5, while the magnitude difference between field 3 and field 5 exceeded 0.2 mag. This photometric difference can be the result of the low number of isolated, bright zeropoint reference stars and the substantial difference in the resolution between the NACO and UKIDSS data.

The higher density in field 3 limits the number of isolated candidates, thus field 3 was calibrated against field 5 in order to adjust all fields to the same zeropoint.

4. Determining Extinction

The extinction of each star can be derived by individual dereddening in the color-magnitude plane. In this section a sample of cluster members is selected from the Color-Magnitude Diagram (CMD) of each field to determine the individual extinction for each cluster star candidate.

The CMD for the central field is shown in Fig. 5. A population of blue foreground sources with lower extinction and mostly associated with the spiral arms, as well as intrinsically red objects like red giants or red clump stars are present in Fig. 5. We applied a color cut (shown as vertical dashed lines in Fig. 5) in order to reject contaminating sources and obtain a representative sample of cluster members. The color cut was done based on the prominent main sequence cluster members in the CMD of the central part of the Arches cluster. The bright part of the observed sequence in the central field, $11 < K < 15$ mag, has the mean color of $H - K_s = A_H - A_{K_s} \sim 1.6$ mag (Fig. 5) which is equal to an approximate color of $J - K \sim 4.4$ mag. Brighter sources, $K < 11$, are likely to belong to the known WR population in the Arches cluster. The guiding color from the field 1, 4.4 mag, and location of bright cluster member candidates in the outskirts CMDs lead us to define the corresponding color-cuts for each outskirt field (Fig. 6). The cluster member candidates in the outskirts CMDs are more extinguished compared to the field 1

(as can be seen in Fig. 6 that the green dot-dashed lines are located at the left side of the black diamonds), which is consistent with previous studies that show the extinction increases outward the cluster center (Stolte et al. 2005; Espinoza et al. 2009).

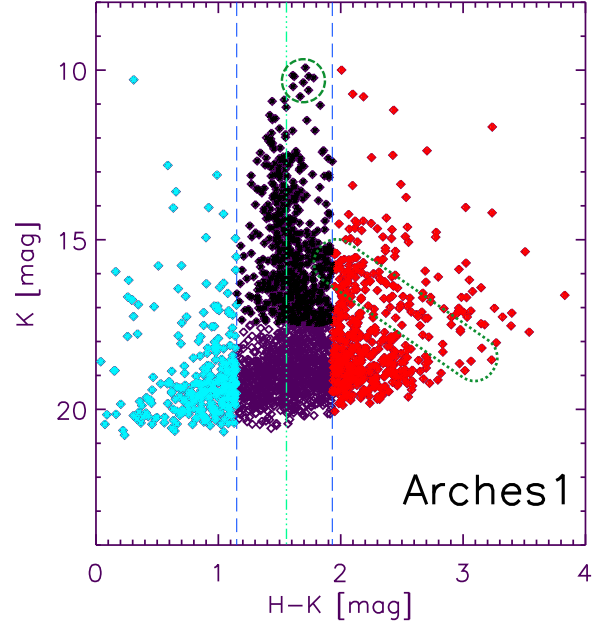


Fig. 5. Color-magnitude diagram of the center of the Arches cluster. Vertical dashed lines show the color-cut used to discard contaminating background and foreground sources. Less extinguished foreground sources, mostly associated with the spiral arms, are shown by blue diamonds whereas intrinsically red objects like red giants or red clump stars (the latter marked with an enclosed dotted line) are illustrated with red diamonds. The black diamonds represent likely cluster members. The mean $H-K$ color of the bright cluster members, $11 < K < 15$ mag, in the center of the Arches cluster is shown by a green dot-dashed line. Brighter sources, $K < 11$ mag, are likely to belong to the known WR population in the Arches cluster (denoted by enclosed dashed line).

The age of the Arches cluster is estimated to be 2.5 Myr (Blum et al. 2001; Najarro et al. 2004; Martins et al. 2008, for a detailed discussion of the previous studies on age and the metallicity of the cluster see Sect. 5.2). We adopted a Geneva isochrone (2001) with solar metallicity located at the GC distance of 8 kpc (Ghez et al. 2008).

In order to derive the individual extinction values we use two extinction laws (EL): Rieke & Lebofsky (1985) and Nishiyama et al. (2009). As mentioned in the introduction, the extinction law derived toward the GC by Rieke & Lebofsky (1985) ($A_\lambda \propto \lambda^{-1.6}$: $\frac{A_J}{A_K} = 2.51, \frac{A_H}{A_K} = 1.55$) was used in most stellar population studies in the GC until recently. Nishiyama et al. (2009) re-derived the extinction law toward the center and obtained a power law of steeper decrease with wavelength ($A_\lambda \propto \lambda^{-2}$: $\frac{A_J}{A_K} = 3.02, \frac{A_H}{A_{K_s}} = 1.73$), which is also consistent with the recent determination of the near-infrared extinction law by Schoedel et al. (2010) and Stead & Hoare (2009).

Using two ELs translates into two extinction path slopes in the CMD (Fig. 7). We slide back the cluster members along each extinction path toward the non-extinguished theoretical isochrone. The brightness, color and mass of a star at the intersection point

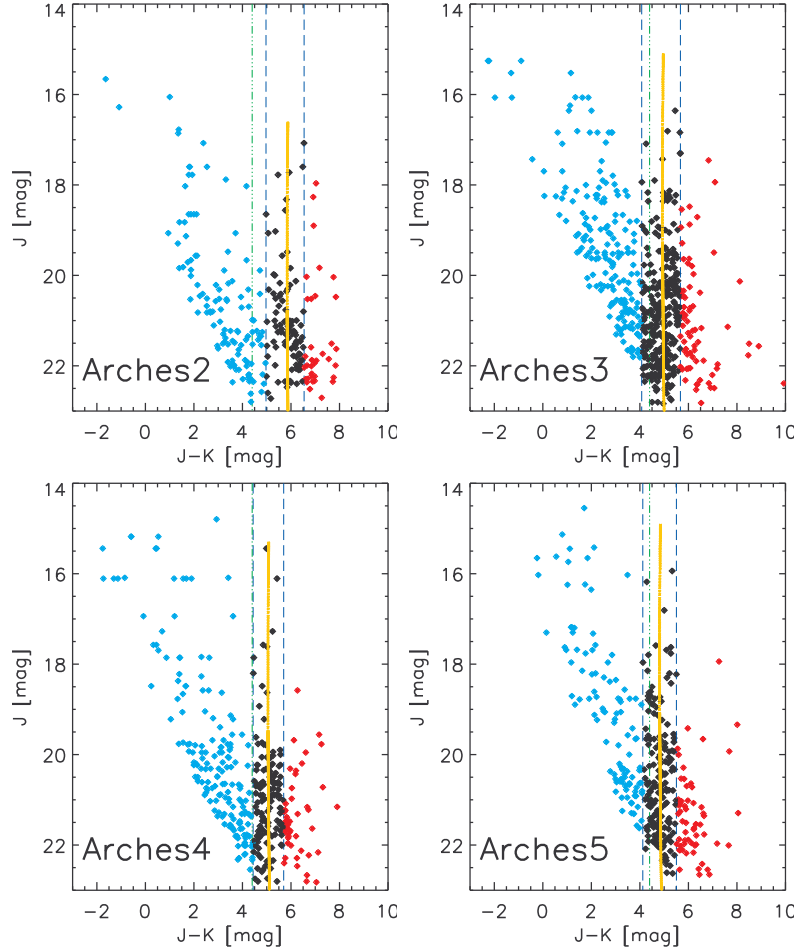


Fig. 6. Color-magnitude diagrams of the outskirts of the Arches cluster. Blue dashed lines show the color-cut used to choose the cluster members and discard background (blue diamonds) and foreground (red diamonds) sources. The Geneva isochrone with the mean extinction value of the cluster members in each field is shown in yellow. The green dot-dashed line represents the approximate mean color of the cluster members in the center of the cluster where the mean extinction is slightly lower.

of the non-reddened isochrone with the extinction vector are assumed to be the intrinsic brightness, color and mass of the star (Fig. 7). In this work we do not consider binarity or rotation of the detected sources which can also partly contribute to the reddening.

4.1. Comparing derived parameters using the two extinction laws

Extinction causes stars to be reddened with respect to their intrinsic color. Assuming different extinction laws will change the derived extinction and consequently the intrinsic properties of the stars. Figure 8 (left) strikingly illustrates the K_s -band extinction difference, ΔA_{K_s} , for each star in field 3 using the Rieke & Lebofsky (1985) EL (RL-EL) and the Nishiyama et al. (2009) EL (N-EL). The A_{K_s} difference across the whole cluster is more than 0.5 mag and it can reach up to 1.1 mag which is equivalent to roughly 10 magnitudes of visual extinction. The difference depends linearly on the extinction being higher for more extinguished sources. The average A_{K_s} difference in the cluster is $\sim 24\%$. The A_{K_s} difference in percentage (right) and absolute value (left) for field 3 is shown in Figure 8. In field 3 most of the sources have an A_{K_s} difference of 25% whereas some fainter sources (red and orange points in Fig. 8) appear in a small upward spread in this

plot. The less certain photometry of fainter sources together with a little curvature at the low-mass end of the isochrone causes this spread: since the length of the connecting path from a star to the isochrone is the measure of the stars' extinction, slightly different slopes of the connecting path results in a bigger difference in the length of the line in areas where the isochrone has a small bend.

Figure 9 shows the difference of the derived initial mass for each star using the two different ELs for field 3. Derived masses using the RL-EL are $\sim 30\%$ higher than derived masses assuming the N-EL across the Arches cluster. While the most massive initial mass in our sample is $104M_{\odot}$ when de-reddening with a RL-EL, the highest initial mass is only 81 when the N-EL is used. In Fig. 9, the less certain photometry of faint sources and a small bend in the faint end of the isochrone act against the more rapid increase of masses at the bright end of the isochrone. Therefore in Fig. 9 there is a vertical spread of a few percent among both faint and bright sources.

4.2. Extinction map

From the individual extinction values we can construct the extinction map. Ideally, we need to have the extinction value for all the points in our field to be able to plot the extinction map.

Since the extinction is just known for the places in which we observe stars, creating the extinction map means assigning each star's extinction value to its neighborhood area. We use Voronoi diagrams to construct the neighborhood of each star on the plane of the sky. If we have a 2-D plane (\mathbb{R}^2) with a finite data set of n sites (stars) $S = \{s_1, s_2, \dots, s_n\}$, the i -th Voronoi cell consists of all points ($x \in \mathbb{R}^2$) whose distance to its generating site, s_i , is not greater than any other site in the plane, $V(s_i) = \{x \in \mathbb{R}^2 \mid \forall j \neq i, d(s_i, x) < d(s_j, x)\}$.

The Voronoi diagram results in a polygon partition of the plane. Over-densities are represented as regions of small area and homogeneously spread points are reflected as polygons with comparable area, while a preferred orientation in the distribution of the points are exhibited as oriented shapes (Aurenhammer & Klein 2000). The resulting extinction map derived assuming the N-EL is shown in Fig. 10. Bright colors correspond to regions of low extinction while dark patches represent high extinction areas. The inverse of the area of each Voronoi cell shows the precession of the extrapolation of the star's extinction to its region. As discussed in Sect. 4.1, using different extinction laws would alter the individual extinction value between 0.5 and 1 mag (see Fig. 8). However, the structure of the extinction map remains very similar by applying different extinction laws since differences in the spatial extinction distribution are small.

The K_s -band extinction derived employing the RL-EL varies between $2.1 < A_{K_s} < 4.4$ mag. In the inner core of the cluster we see on average $\langle A_{K_s} \rangle (r < 0.2 \text{ pc}) = 2.8$ mag, as compared to a mean extinction of $\langle A_{K_s} \rangle (0.2 < r < 0.4 \text{ pc}) = 2.9$ mag in the intermediate annulus and $\langle A_{K_s} \rangle (r > 0.4 \text{ pc}) = 3.4$ mag in the cluster's outskirts. The largest extinction is found in the south-west of the cluster (field 2) while the least extinction is detected toward the center (field 1). The acquired extinction values applying the N-EL are on average 0.76 mag less than values derived based on the RL-EL. The extinction derived from the N-EL varies within the range of $1.6 < A_{K_s} < 3.3$ mag. The mean extinction values across the inner region of $r < 0.2 \text{ pc}$, the annulus with $0.2 < r < 0.4 \text{ pc}$ and the region of $0.4 < r < 1.5 \text{ pc}$ are, respectively, 2.1, 2.2 and 2.5 mag.

The derived values of A_{K_s} using the Rieke & Lebofsky (1985) EL are consistent with the only previous study with individual extinction correction for the Arches cluster by Espinoza et al. (2009). This study used the Fitzpatrick (2004) EL and either a Bayesian or CMD Sliding method to derive extinction values depending on brightness and availability of JHK_s photometry of each star. They found a K_s -band extinction range of $2.13 < A_{K_s} < 4.14$ mag across a field of view which extends $\sim 0.5 \text{ pc}$ from the cluster center. They have found a mean extinction value of $\langle A_{K_s} \rangle = 2.97$ in the inner core ($r < 0.2 \text{ pc}$) followed by a mean extinction value of $\langle A_{K_s} \rangle = 3.18$ in the region of $0.2 < r < 0.4 \text{ pc}$. Espinoza et al. (2009) cover the cluster beyond the distance of 0.5 pc partly toward the north and west, where they report a mean extinction of $\langle A_{K_s} \rangle = 3.24$ for this area (see Espinoza et al. 2009, Fig. 12). These results are consistent with our findings of 2.8, 2.9 and 3.4 mag for similar regions based on the Rieke & Lebofsky (1985) EL which is comparable to Fitzpatrick (2004).

In a recent study, Dong et al. (2012) also calculate individual extinction values for a number of massive stars in the GC, including 19 sources within a radius of one parsec of the Arches cluster (see Table 2 in Dong et al. 2012). The extinction values are derived using the broad-band filters (J, H and K_s) of SIRIUS (Nagayama et al. 2003) and by employing the extinction law by Nishiyama et al. (2006). The mean value of the derived individual A_{K_s} extinctions for these 19 sources is 2.53 which is

Table 2. The minimum star mass which is included in the mass function list. The low-mass cut is slightly different in the center since the observation set-up and completeness limit is different for the center (as explained in Sect. 2).

Field	N-EL	RL-EL
min mass-cut: center	$12.5 M_{\odot}$	$17.5 M_{\odot}$
min mass-cut: outskirts	$9.7 M_{\odot}$	$13.6 M_{\odot}$

consistent within 0.16 mag with our N-EL based mean extinction $\langle A_{K_s} \rangle (r < 1 \text{ pc}) = 2.37$.

The region of low extinction in the center of the cluster is probably due to the presence of massive stars. Massive stars provide strong UV radiation and stellar wind that can swipe up the medium from gas and dust (see Stolte et al. 2002). Identified X-ray sources which coincide with radio emission in the Arches cluster also confirm the existence of powerful ionized winds from late type Of/Wolf-Rayet stars in the center of the cluster (Lang et al. 2001; Law & Yusef-Zadeh 2003). Regions of higher extinction in the south west and north west of the cluster coincide with dark lanes visible in the JHK composite from the UKIDSS GPS survey (Lucas et al. 2008). Espinoza et al. (2009) also found an area of higher extinction toward the south-west of the cluster which lies in the gap between fields 1 and 2 in our work. The presence of relatively low extinction areas in the east part of the outer cluster region is consistent with identified diffuse x-ray emission of the cluster which is elongated towards this area (Law & Yusef-Zadeh 2003).

Apart from the overall trend of having lower extinction values toward the center of the cluster, we observe quite patchy extinction both in the center and outskirts of the cluster. The extinction varies by ~ 2 mag in A_{K_s} across the cluster ($\Delta A_{K_s, RL-EL} = 1.81$, $\Delta A_{K_s, N-EL} = 2.32$) which is equivalent to roughly 15-20 mag of visual extinction. Such a high and variable extinction (as was shown earlier for the center of the cluster by Espinoza et al. 2009) implies that using global extinction trends or even single extinction values derived by averaging individual measurements would alter the results for the Arches cluster systematically.

5. Mass function

To derive the present-day mass function (PDMF) of the cluster we applied a more conservative low-mass cut on top of the criteria imposed by sensitivity (explained in Sect. 2). We discarded all the sources whose masses are less than the mass of the reddest source with a luminosity close to the sensitivity limit. This criterion ensures that the mass function is complete in the faintest mass bin, and corresponds to an extinction-limited sample. The lowest mass included in the PDMF is $10\text{-}17 M_{\odot}$ depending on the field and the extinction law which is applied (see Table 2). Cutting the low mass end of the mass distribution helps to avoid the field contamination which is dominated by K and M giants in the galactic bulge for stars fainter than $J \sim 21$ mag. This is crucial for the outskirts of the cluster where we expect to have more contamination by field stars relative to the decreasing number of cluster members.

To avoid the bias resulting from the number of stars per bin and its assigned weight in the derivation of the PDMF slope, we utilize the binning method described by Maíz Apellániz & Ubeda (2005). Following this method we allow for dynamic bin sizes so that each bin contains approximately the same number

Table 3. Acquired slopes for the present-day mass function derived from initial and present-day masses of the Arches cluster applying Nishiyama et al. (2009) (N-EL) and Rieke & Lebofsky (1985) (RL-EL) extinction laws. The slopes are calculated for the three different regions distinguished by the distance from the cluster center. Since our observation does not cover the whole outer annulus of $0.4 < r < 1.5$ pc, we have scaled the number of sources in this region to the area of the outer annulus which is covered by the observed fields. The last row contains the same numbers for the whole cluster up to a radius of 1.5 pc.

region (pc)	Nishiyama et al. (2009) EL		Rieke & Lebofsky (1985) EL	
	PDMF, init	PDMF, P-D	PDMF, init	PDMF, P-D
$r < 0.2$	-1.86 ± 0.19	-1.76 ± 0.22	-1.92 ± 0.2	-1.63 ± 0.24
$0.2 < r < 0.4$	-2.26 ± 0.21	-2.23 ± 0.27	-2.18 ± 0.22	-2.05 ± 0.28
$0.4 < r < 1.5$	-2.93 ± 0.19	-2.95 ± 0.26	-2.87 ± 0.19	-2.78 ± 0.27
$r < 1.5$	-2.53 ± 0.15	-2.52 ± 0.27	-2.48 ± 0.15	-2.29 ± 0.27

of stars and hence the same statistical weight (for details about the implementation of this method see Hußmann et al. 2012).

Figure 11 shows the derived PDMFs of the Arches cluster in logarithmic scale such that a standard Salpeter mass function (1955) is a line with a slope of $\alpha = -2.35$. The PDMFs are well represented by a single slope power-law function ($\frac{dN}{dm} \propto m^{-\alpha}$) at all radii. The black (red) lines show the mass distribution and fitted power laws for the RL-EL (N-EL). The PDMF of the cluster is plotted in three different regions: the inner core with $r < 0.2$ pc, the intermediate annulus of $0.2 < r < 0.4$ pc and the outskirts which cover partly the outer annulus with $0.4 < r < 1.5$ pc. Since our fields (see Fig. 2) do not cover the whole area of the outer annulus, $0.4 < r < 1.5$ pc, the number of sources in each mass-bin is scaled to the observed ratio of the outer annulus area. The projected distances of 0.2 pc and 0.4 pc from the cluster center are the estimated core and half mass radius of the cluster, respectively (Figer, McLean & Morris 1999; Stolte et al. 2002; Harfst et al. 2010). Most of the previous studies used these annuli to report the mass function slopes. The radius of 1.5 pc is chosen to cover the cluster out to its tidal radius. For a detailed discussion about the tidal radius of the Arches cluster see Sect. 5.1.

The derived slopes using the two extinction laws (Fig. 11) show that changes in the slope of the fitted power-law function due to the extinction law are similar to the fitting uncertainty (for the detailed description of the systematic and the random errors of the derived slopes see Sect. 5.2). However, the choice of the extinction law applied for the individual de-reddening of each star alters the shape, particularly the lower and the upper mass limit of the resulting MF. Changing the boundaries of the mass function translates to shifting the highest observed mass to lower values. This is crucial as the Arches cluster is not expected to have had any supernova at its present age. As the cluster is believed to cover the full mass range, it was used to derive a possible upper-mass limit of $M = 150M_{\odot}$ for the star formation process in the Milky Way (Figer 2005). Such an upper mass limit has severe implications on our understanding of the stellar evolution and the formation of the highest mass stars. While the most massive initial mass in our sample is $104M_{\odot}$ when de-reddening with a RL-EL, the highest initial mass is only $81M_{\odot}$ when the N-EL is used. This suggests that the claimed upper-mass strongly depends on the choice of the extinction law and should be revisited with the steeper extinction laws found toward the GC in the past few years. Such an investigation is beyond the scope of this paper.

We obtain a PDMF slope of $\alpha_{Nishi} = -1.76 \pm 0.22$ in the cluster core ($r < 0.2$ pc) (see Fig. 11, upper left). In the intermediate annulus of $0.2 < r < 0.4$ pc the slope of the PDMF reaches $\alpha_{Nishi} = -2.23 \pm 0.27$ which is in the range of the standard Salpeter mass function (1955) with $\alpha = -2.35$, (Fig. 11, upper

right). The number of massive stars compared to low mass stars continues to decrease in the outskirts of the cluster. We found a high mass depleted PDMF for the outer annulus of the cluster, $0.4 < r < 1.5$ pc with a slope of $\alpha_{Nishi} = -2.95 \pm 0.26$ (Fig. 11, lower left).

A flattening of the Arches mass function toward the center has been shown in previous studies. Stolte et al. (2005) found a slope of -1.26 for the mass range of $10M_{\odot} < M < 63M_{\odot}$ in the inner core. This study corrected for a systematic radial extinction variation. Individual extinction corrections by Espinoza et al. (2009) resulted in a slope of -1.88 in the cluster core³.

Our finding, $\alpha_{Nishi} = -2.23 \pm 0.27$, in the intermediate annulus is consistent with the slope Espinoza et al. (2009) found, -2.28 , in this region for stars above $10M_{\odot}$. Kim et al. (2006) corrected for a single extinction value and found a steeper slope of -1.71 in this annulus ($0.2 < r < 0.35$ pc) for the stars in the massive range only ($5M_{\odot} < M < 50M_{\odot}$).

Although there is no reported slope for the outskirts of the cluster in the previous studies, we can compare our result with simulations. Harfst et al. (2010) performed a series of N-body simulations to find the best model and initial conditions to reproduce the observed data of the Arches cluster. They constructed the mass function for the best fitting models which have a King model concentration parameter of $W_0 = 3$ and consist of one model with a flat initial mass function (IMF) and three with a Salpeter IMF (see Fig. 12). Although the models with the Salpeter IMF are more consistent with the observed slopes, nevertheless all the models exhibit a flattening toward the center. The three Salpeter and the one flat IMF model deviate primarily at larger radii ($r > 0.4$ pc) where the predicted slope difference is 0.5 dex. The derived slope from a Salpeter IMF model by Harfst et al (2010) at the radius of 1 pc is $\alpha \sim -3$ which is in good agreement with our finding of $\alpha_{Nishi} \sim -2.95 \pm 0.26$ in the outskirts of the cluster (Fig. 12). This picture is consistent with the dynamical evolution of the cluster which has competed the primordial mass segregation scenario as the reason of the observed mass segregation of the Arches cluster. Obtaining the combined PDMF including all the sources within our fields up to ~ 1.5 pc yields a slope of $\alpha_{Nishi} = -2.52 \pm 0.27$ similar to the Salpeter IMF (see Fig. 11).

Integrating the PDMF across the desired mass range yields the total mass of the cluster. The complete PDMF ($r < 1.5$ pc) of the cluster with a slope of $\alpha_{Nishi} = -2.52 \pm 0.27$ was integrated over the mass range of $1 - 66 M_{\odot}$, yielding a total mass of $M_{cl} = (1.8^{+0.4}_{-0.3}) \times 10^4 M_{\odot}$ for the Arches cluster. This value is comparable within the uncertainty with the dynamical total

³ Espinoza et al. (2009) used initial instead of present-day stellar masses to derive the mass function. The comparable slopes to Espinoza et al. (2009) (derived from initial masses) are illustrated in Table 3.

mass estimate of the cluster. Clarkson et al. (2012) measured the dynamical mass from the cluster's velocity dispersion to be $M_{cl}(r < 1.0 pc) = 1.5_{-0.6}^{+0.74} \times 10^4 M_{\odot}$ for the Arches cluster. Previous studies estimated ~ 2 times higher photometric mass for the cluster. However, their results are not directly comparable to our numbers since they have calculated over a narrower annulus (eg. Espinoza et al. 2009). The discrepancy can be due to an extrapolation which is based on the slopes derived from the center of the cluster ($r < 0.4 pc$) and has resulted to overestimating the number of higher mass sources in the outskirts.

5.1. Tidal radius of the cluster

The projected distance of the Arches cluster is $\sim 25 pc$ from the GC, however since the Galactic mass distribution and the location of the cluster along the line of sight is not determined, it is not easy to estimate the true tidal radius of the cluster. Kim et al. (2000) estimated the tidal radius of the cluster based on a power law approximation of Galactic mass inside a Galactocentric radius, r_g . Their comparison between the simulated projected number density and the observed mass functions at the time did not rule out a Galactic distance r_g of 20 and 50 pc for the Arches cluster, but favored $r_g = 30 pc$ which results in a tidal radius of $\sim 1 pc$. A similar study by Portegies Zwart et al. (2002) concluded that in order to reproduce the observed density within the half-mass radius, the Arches cluster should lie at the distance of 50-90 pc from the Galactic center which result in a tidal radius of 1.6-2.5 pc (see Portegies Zwart et al. (2002), their Table 4).

A more recent study by Launhardt et al. (2002) estimates the enclosed mass in the inner 500 pc of the Milky way. This observational study showed that the potential in the inner Galaxy cannot be modeled with a single power law and takes into account the mass contribution of the nuclear stellar cluster, the nuclear stellar disk, the central black hole, the Galactic bulge and the interstellar mass in the nuclear bulge (see Launhardt et al. 2002, Fig. 14). Applying the enclosed mass from the Launhardt et al. (2002) model, M_g , for the Galactocentric range of $r_g = 30-100 pc$ and a cluster mass of $M_{cl} \sim 20000 M_{\odot}$ yields a tidal radius, r_t , of 1.3 – 2.5 pc:

$$r_t = \left(\frac{M_{cl}}{2 \times M_g} \right)^{1/3} \times r_g \approx 1.3 - 2.5 pc$$

We observe the Arches cluster out to 1.5 pc which is in the range of the derived tidal radius.

5.2. Uncertainties of the mass function slopes

The uncertainties of the PDMF slopes illustrated in Fig. 11 represent the numerical fitting uncertainties ($\sigma_{fit} \sim 0.18$). There are also systematic errors which contribute to the final estimated uncertainty of the PDMF slopes. One source of systematic uncertainty originates from the cluster age, metallicity and the corresponding choice of the isochrone. Studies determining the age of the Arches cluster are based on spectroscopy of Nitrogen rich (WN) Wolf-Rayet stars (WRs) and O super-giants, along with the absence of carbon rich WR stars which establish an upper limit for the age of the cluster. Although studies agree on a narrow evolutionary spread and subsequently a narrow age spread among the cluster stars, it is still hard to confine the absolute age of the Arches cluster. Blum et al. (2001) studied $2 \mu m$ narrow band images and derived an age of 2-4 Myr assuming the stars are of WR type. Najarro et al. (2004) analysed spectra of five massive stars (classified as 3 WNLs and 2 O stars) and obtained an age of 2-2.5 Myr. They derived solar metallicity for all the five sources based on measuring their N abundances. More re-

cent work by Martins et al. (2008) used *K*-band spectra of 28 bright stars in the cluster. The age of 2-3 Myr was obtained for WN7-9 stars while some O super-giants could have ages up to 4 Myr. They suggested that lighter elements are probably slightly super-solar though iron peak elements show solar metallicity. Espinoza et al. (2009) built mass functions using different ages (2-3.2 Myr) and show that the uncertainty from the choice of age or metallicity will add an uncertainty of $\sigma_{iso} \sim 0.1 dex$. This result is in agreement with Hußmann et al. (2012) who applied different isochrones (3-5 Myr) to construct the PDMF of the Quintuplet cluster.

The second significant source of uncertainty originates from the choice of the extinction law (see Sect. 4). We conclude that if none of the extinction laws can be disregarded based on the scientific discussion, an uncertainty of 0.17 dex should be considered as a result of the choice of the extinction law (see Fig. 11 and Table 3). Applying the steeper extinction laws (Nishiyama et al. 2009; Schoedel et al. 2010; Stead & Hoare 2009) steepens the slope of the PDMF by 0.13 – 0.23 dex (see Fig 11). It is important to notice that this 0.17 dex is a systematic uncertainty. Although all the sources of random and systematic errors are detached and reported above (listed in Table 3), for the sake of comparison with previous studies with different assumptions about the extinction law and the age of the cluster, we consider a quadratic sum of random and systematic errors of $\sim 0.26 dex$ as a result of all the uncertainties discussed above ($\sigma_{fit}, \sigma_{iso}, \sigma_{EL}$).

6. Conclusions

We present a quantitative study on the effect of the applied extinction law on the derivation of the present-day mass function in young massive star clusters using the Arches cluster as a template. We show how the choice of the near-infrared extinction law influences the absolute values of the patchy extinction toward the star clusters in the Galactic Center, and how it affects the slope of the present-day mass function. We also derive the present-day mass distribution of the outskirts of the cluster for the first time to obtain a full understanding of the cluster mass distribution up to its tidal radius. *K_s* and *H*-band AO images taken by the VLT as well as *J*-band images obtained by Subaru are analyzed for this investigation. The main findings of our study are:

1. The extinction law derived by Rieke & Lebofsky (1985), $\propto \lambda^{-1.61}$, was used commonly in previous studies toward the Arches cluster. We compare the results obtained from Rieke & Lebofsky (1985) to the results acquired assuming the extinction law derived by Nishiyama et al. (2009), as several recent studies toward the GC yield steeper wavelength dependence of $\propto \lambda^{-2}$ for the near-infrared extinction. Applying these different extinction laws results in an average systematic extinction difference of $\Delta A_{K_s} = 0.76 mag$, ($\sim 24\%$) which can reach up to 1.1 mag. The obtained average extinction values applying the Nishiyama et al. EL are 2.1, 2.2, 2.5 mag for the three investigated cluster annuli of $r < 0.2 pc$, $0.2 < r < 0.4 pc$ and $0.4 < r < 1.5 pc$, respectively. Applying the Rieke & Lebofsky EL increases the average extinction values to 2.8, 2.9 and 3.4 mag for the same three regions.
2. The extinction map derived by individual de-reddening of the cluster member candidates shows a high and variable extinction across the cluster. The derived extinction values applying the Nishiyama et al. (2009) extinction law and Rieke & Lebofsky (1985) vary within the range of $1.6 < A_{K_s} < 3.3$

Table 4. Source list. From left to right the columns are: Sequential ID for stars, R.A. offset from the reference star which is the source with ID 6 (R.A.=17:45:50.046 , Dec. = -28:49:23.62), DEC. offset from the reference star, measured J -band and K_s -band brightness along with the photometric uncertainties (columns 4-6), estimated K_s -band extinction applying the RL-EL (column 7) and the N-EL (column 8), present-day mass applying the RL-EL (column 8) and the N-EL (column 10), initial mass applying the N-EL, cluster field which the detected source belongs to.

ID	$\Delta R.A.$ (sec)	$\Delta Dec.$ (sec)	J (mag)	K_s (mag)	σ_{K_s}	$A_{K_s(RL-EL)}$ (mag)	$A_{K_s(N-EL)}$ (mag)	$PD - mass_{RL-EL}$ M_\odot	$PD - mass_{N-EL}$ M_\odot	$I - mass_{N-EL}$ M_\odot	field
1	-0.015	-0.200	12.869	11.03	0.006	3.32	2.56	65.2	60.6	66.7	1
2	-0.435	0.207	12.64	11.0	0.006	2.83	2.18	62.0	56.1	5.7	1
3	-0.694	0.333	12.74	11.32	0.023	2.59	2.00	58.1	49.6	51.7	1
4	-0.388	0.399	12.88	11.42	0.006	2.67	2.06	57.5	49.6	5.7	1
5	-0.654	0.282	12.90	11.45	0.005	2.63	2.03	56.8	47.8	49.7	1
6	0	0	13.201	11.47	0.007	3.13	2.41	61.6	53.7	56.7	1

The complete table of the sources will be published in the electronic edition of the A&A journal.

mag and $2.8 < A_{K_s} < 4.21$ mag, respectively. The patchiness of the extinction is high and hardly follows any trend; nevertheless, a region of relatively low extinction is present toward the center of the cluster. An area of high extinction is located in the south west and partly north west of the cluster.

- Obtained stellar masses assuming the Nishiyama et al. (2009) extinction law are $\sim 30\%$ less massive than derived masses assuming the formerly used extinction law by Rieke & Lebofsky (1985). Considering that the Arches cluster hosts a collection of high mass-stars a mass difference of $\sim 30\%$ can change the estimated individual initial masses substantially. In this work, the upper mass limit decreases from an initial mass of $104 M_\odot$ to $81 M_\odot$ when using the steeper extinction law, which has severe implications on the discussion of the possible maximum stellar mass forming in the Milky-Way (see Sect. 5 for a detailed discussion).
- We derive the present-day mass function of the cluster for an area which approximately reaches to the tidal radius of the cluster. Our mass functions cover the massive part of the mass spectrum (see Table 2) and are obtained in three different annuli of $r < 0.2$ pc (core), $0.2 < r < 0.4$ pc (intermediate annulus) and $0.4 < r < 1.5$ pc (outer annulus). The slopes derived assuming the Nishiyama et al. (2009) extinction law are increasing from a flat slope of $\alpha_{Nishi} = -1.76 \pm 0.22$ in the core to $\alpha_{Nishi} = -2.23 \pm 0.27$ in the intermediate annulus and become as steep as $\alpha_{Nishi} = -2.95 \pm 0.26$ in the outer annulus. For the sake of comparison we consider the quadratic sum of random and systematic error, 0.26 dex, as a result of all the uncertainties but it is important to notice that uncertainties from the assumption of the extinction law and the age of the cluster are systematic errors. The slope derived by applying the Rieke & Lebofsky (1985) EL are on average smaller by 0.17 dex. Our mass functions shows that while in the core of the cluster the number of massive stars compared to lower mass stars are high relative to the normal Salpeter mass function ($\alpha = -2.35$, 1955), the intermediate annulus has a Salpeter like distribution and the outskirts are high-mass depleted. Comparing the mass function slope in the outer annulus of the cluster with N-body simulations performed by Harfst et al. (2010), we conclude that the observed slopes are consistent with dynamical evolution of a cluster which formed with a normal Salpeter IMF.

The extrapolation of the complete PDMF for the area of $r < 1.5$ pc, derived for a present-day mass range of $1-66 M_\odot$ and a slope of $\alpha_{Nishi} = -2.52 \pm 0.27$ results in a to-

tal mass of $M_{cl} = (1.8_{-0.3}^{+0.4}) \times 10^4 M_\odot$ for the Arches cluster, which is consistent within the uncertainty with the previous dynamical total mass estimate of the cluster by Clarkson et al. (2012).

It was argued before that the IMF might be top-heavy in the GC due to increased could temperatures and magnetic fields (Morris 1993, see also Klessen et al. 2007 and Stolte et al. 2005 for discussions). The slopes derived in our analyses are consistent with the expectations of the dynamical evolution of the cluster starting with a Salpeter IMF at birth. Hence we do not need to invoke a primordially deviating mass function to explain the spatial distribution of the stars in the Arches cluster.

Acknowledgements. M.H., B.H. and A.S. acknowledge funding from the German science foundation (DFG) Emmy Noether program under grant STO 496-311, and thank the Argelander-Institute for Astronomy at the University of Bonn for being such a generous host. It is a pleasure to thank the NAOS-CONICA instrument team for their extensive support during the observations.

References

- Aurenhammer, F., Klein, R., Voronoi diagrams. In Handbook of Computational Geometry, Chapter V, J. Sack and G. Urrutia, editors, pages 201-290. Elsevier Science Publishing, 2000. [SFB Report F003-092, TU Graz, Austria, 1996]. (Gzipped PostScript, 101 p., 473 KB).
- Blum, R.D., Schaerer, D., Pasquali, A., et al. 2001, AJ, 122, 1875
- Cardelli, J. A., Clayton, G. C., & Mathis, J. S., 1989, ApJ, 345, 245
- Clarkson, W. I., Ghez, A. M., Morris, M. R., et al. 2012, ApJ, 751, 132
- Diolaiti, E., Bendinelli, O., Bonaccini, D., et al. 2000, A&AS, 147, 335
- Dong, H., Wang, Q. D., Morris, M. R. 2012, arXiv:1204.6298
- Espinoza, P., Selman, F. J., & Melnick, J. 2009, A&A, 501, 563
- Figer DF, McLean IS, Morris M. 1999. ApJ. 514, 202
- Figer, D. F., Kim, S. S., & Morris, M. et al. 1999, ApJ, 525, 750
- Figer, D. F. 2004, in The Formation and Evolution of Massive Young Star Clusters, ed. H. J. G. L. M. Lamers, L. J. Smith, & A. Nota, ASP Conf. Ser., 322, 49
- Figer D. F., 2005, Nat, 434, 192
- Fitzpatrick, E. 2004 in ASP Conf. Ser. 309: Astrophysics of Dust, ed. A. N. Witt, G. C. Clayton & B. T. Draine, 33-56
- Fruchter, A. S., & Hook, R. N. 2002, PASP, 114, 144
- Ghez, A. M., Salim, S., Weinberg, N. N., et al. 2008, ApJ, 689, 1044
- Harfst, S., Portegies Zwart, S., & Stolte, A. 2010, MNRAS, 409, 628
- HuBmann, B., Stolte, A., Brandner, W., Gennaro, M., & Liermann, A. 2012, A&A, 540, A57
- Iye, M., Karoji, H., Ando, H., et al. 2004, PASJ, 56, 381
- Kim S. S., Figer D. F., Lee H. M., Morris M., 2000, ApJ, 545, 301
- Kim, S. S., Figer, D. F., Kudritzki, R. P., & Najarro, F. 2006, ApJ, 653, L113
- Klessen, R. S., Spaans, M., & Jappsen, A.-K. 2007, MNRAS, 374, L29
- Lang, C. C., Goss, W. M., & Rodriguez, L. F. 2001, ApJ, 551, L143 (LGR01)
- Lang, C. C. 2004, The Formation and Evolution of Massive Young Star Clusters, 322, 179

- Launhardt, R., Zylka, R., Mezger, P.G. 2002, *Astron. Astrophys.* 384, 112
- Lawrence, A., Warren, S. J., Almaini, O., et al. 2007, *MNRAS*, 379, 1599.
- Law, C. & Yusef-Zadeh, F. 2003, *Astron. Nachr.*, Vol. 324, No. S1 (2003)
- Lebofsky, M. J. 1979, *AJ*, 84, 324
- Lejeune, T., Schaerer, D. 2001, *A&A*, 366, 538
- Lenzen, R., Hartung, M., Brandner, W., et al. 2003, in Presented at the Society of Photo-Optical Instrumentation Engineers (SPIE) Conference, Vol. 4841, Society of Photo-Optical Instrumentation Engineers (SPIE) Conference Series, ed. M. Iye & A. F. M. Moorwood, 944952
- Lucas et al., 2008, *MNRAS*, 391, 136
- Lutz, D., Feuchtgruber, H., Genzel, R., et al. 1996, *A&A*, 315, L269
- Mafz Apellániz, J., & beda, L. 2005, *ApJ*, 629, 873
- Martins, F., Hillier, D. J., & Paumard, T. et al. 2008, *A&A*, 478, 219
- Morris, M. 1993, *ApJ*, 408, 496
- Morris, M. & Serabyn, E. 1996, *ARA&A*, 34, 645
- Motohara, K., et al. 2002, CISCO: Cooled Infrared Spectrograph and Camera for OHS on the Subaru Telescope, *PASJ*, 54, 315
- Nagayama, T., Nagashima, C., Nakajima, Y. et al. 2003, *SPIE*, 4841, 459N
- Najarro, F., Figer, D.F., Hillier, D.J., & Kudritzki, R. P. 2004, *ApJ*, 611, L105
- Nishiyama, S., et al. 2006, *ApJ*, 638, 839
- Nishiyama, S., Tamura, M., Hatano, H., et al. 2009, *ApJ*, 696, 1407
- Portegies Zwart, S. F., Makino, J., McMillan, S. L. W., & Hut, P. 2002, *ApJ*, 565, 265
- Rieke, G. H. & Lebofsky, M. J. 1985, *ApJ*, 288, 618
- Rieke, G. H., Rieke, M. J., & Paul, A. E. 1989, *ApJ*, 336, 752
- Rousset, G., Lacombe, F., Puget, P., et al. 2003, in Presented at the Society of Photo-Optical Instrumentation Engineers (SPIE) Conference, Vol. 4839, Society of Photo-Optical Instrumentation Engineers (SPIE) Conference Series, ed. P. L. Wizinowich & D. Bonaccini, 140149
- Salpeter, E. E. 1955, *ApJ*, 121, 161
- Schoedel, R., Najarro, F., Muzic, K., & Eckart, A. 2010, *A&A*, 511, A18+
- Stead, J. & Hoare, M. 2009, *MNRAS*, 400, 731
- Stolte, A., Grebel, E. K., Brandner, W., & Figer, D. F. 2002, *A&A*, 394, 459
- Stolte, A. 2003, Ph.D. thesis, Univ. Heidelberg
- Stolte, A.; Brandner, W.; Grebel, E.; Lenzen, R.; Lagrange, A 2005 *ApJ* 628L 113
- Tody, D. 1993, in ASP Conf. Ser. 52, *Astronomical Data Analysis Software and Systems II*, ed. R. J. Hanish, R. J. V. Brissenden, & J. Barnes (San Francisco: ASP), 173
- Williams J. P., Blitz L., McKee C. F., 2000, *Protostars and Planets IV*, pp 97
- Whittet, D. C. B., et al. 1997, *ApJ*, 490, 72
- Yusef-Zadeh, F., Law, C., Wardle, M. et al. 2002, *ApJ*, 570, 665
- Yusef-Zadeh, F., et al. 2009, *ApJ*, 702, 178

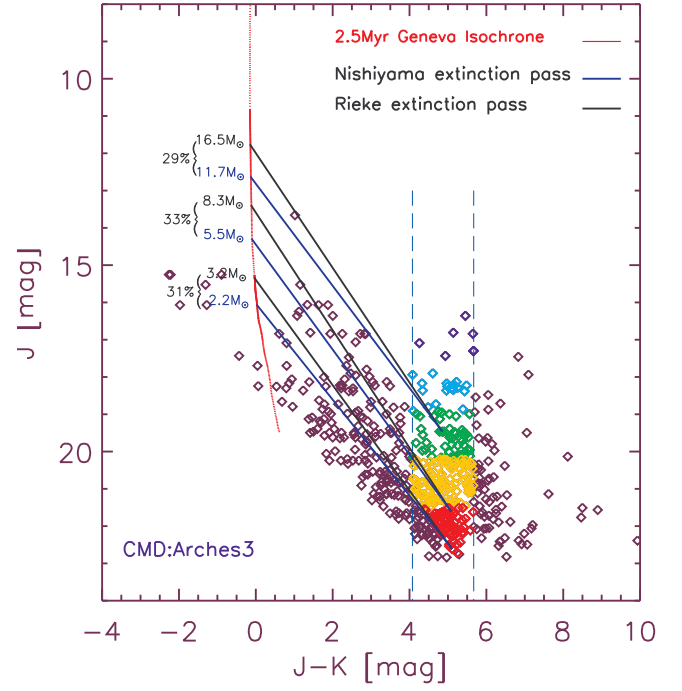


Fig. 7. The Color-magnitude diagram of field 3 in the outskirts of the Arches cluster: cluster members are selected between the two dashed lines and are color coded according to their J -band magnitude. A Geneva isochrone of solar metallicity and age of 2.5 Myr is shown in the plot. Black lines represent the extinction path assuming the Rieke & Lebofsky extinction law (1985) while blue lines are extinction paths based on the Nishiyama et al. (2009) extinction law. The difference of derived masses using the two laws are written for sample sources close to the isochrone in percentage.

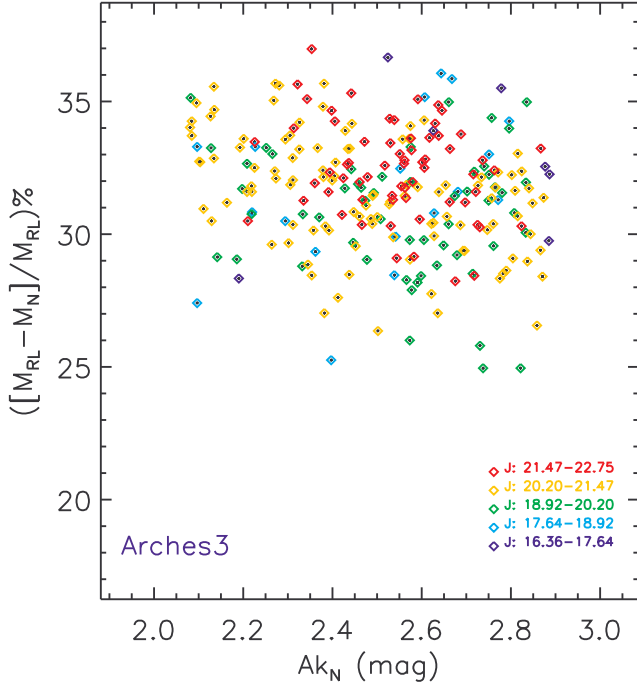


Fig. 9. The derived mass difference assuming the Nishiyama et al. (2009) and Rieke & Lebofsky (1985) extinction laws plotted over A_{K_s} of each source. Derived masses using the Rieke & Lebofsky extinction law are an average 30% larger than derived masses by using the Nishiyama et al. extinction law.

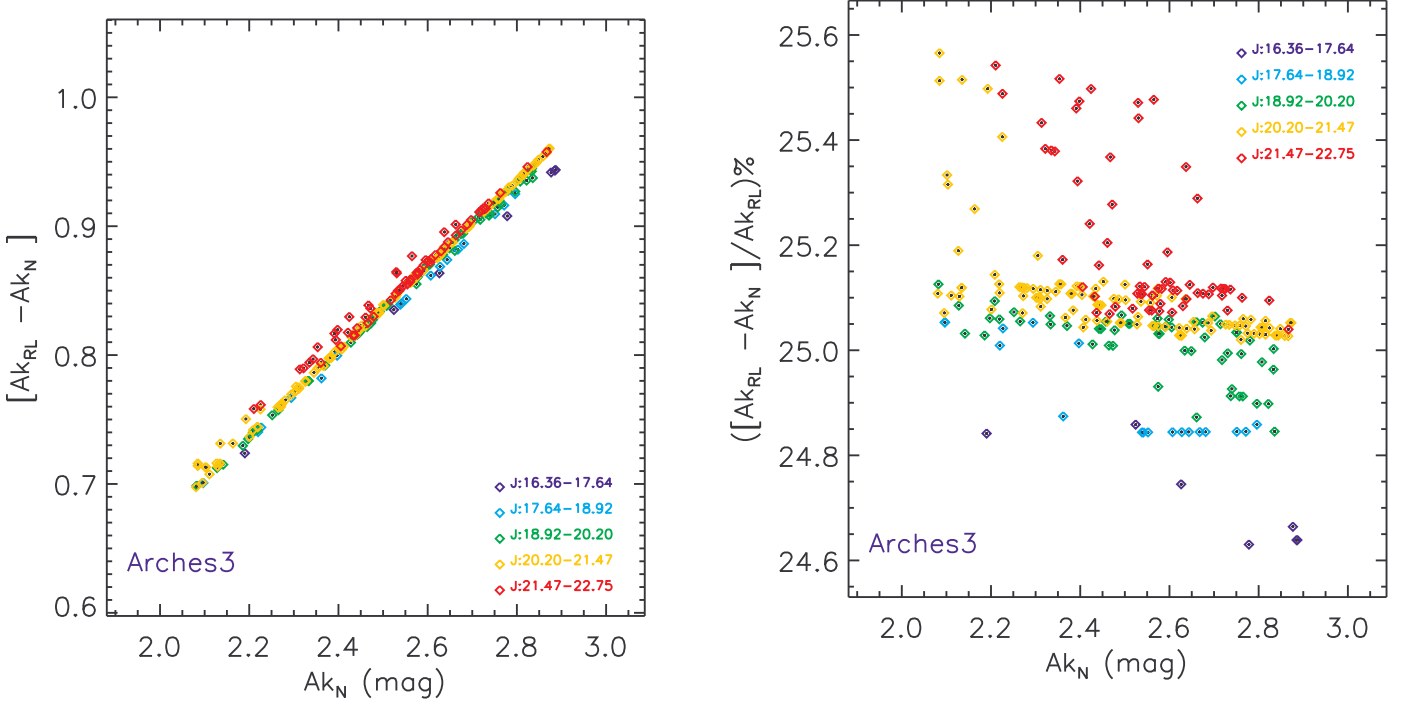


Fig. 8. (a) The extinction difference in field 3 (outskirts of the cluster) derived using the Nishiyama et al. (2009) and the Rieke & Lebofsky (1985) extinction laws plotted over K_s -band extinction derived assuming the Nishiyama et al. extinction law. The difference depends linearly on the extinction increasing with increasing extinction. (b) The difference in percentage. The average A_{K_s} difference is $\sim 25\%$ in field 3 and $\sim 24\%$ across the whole cluster.

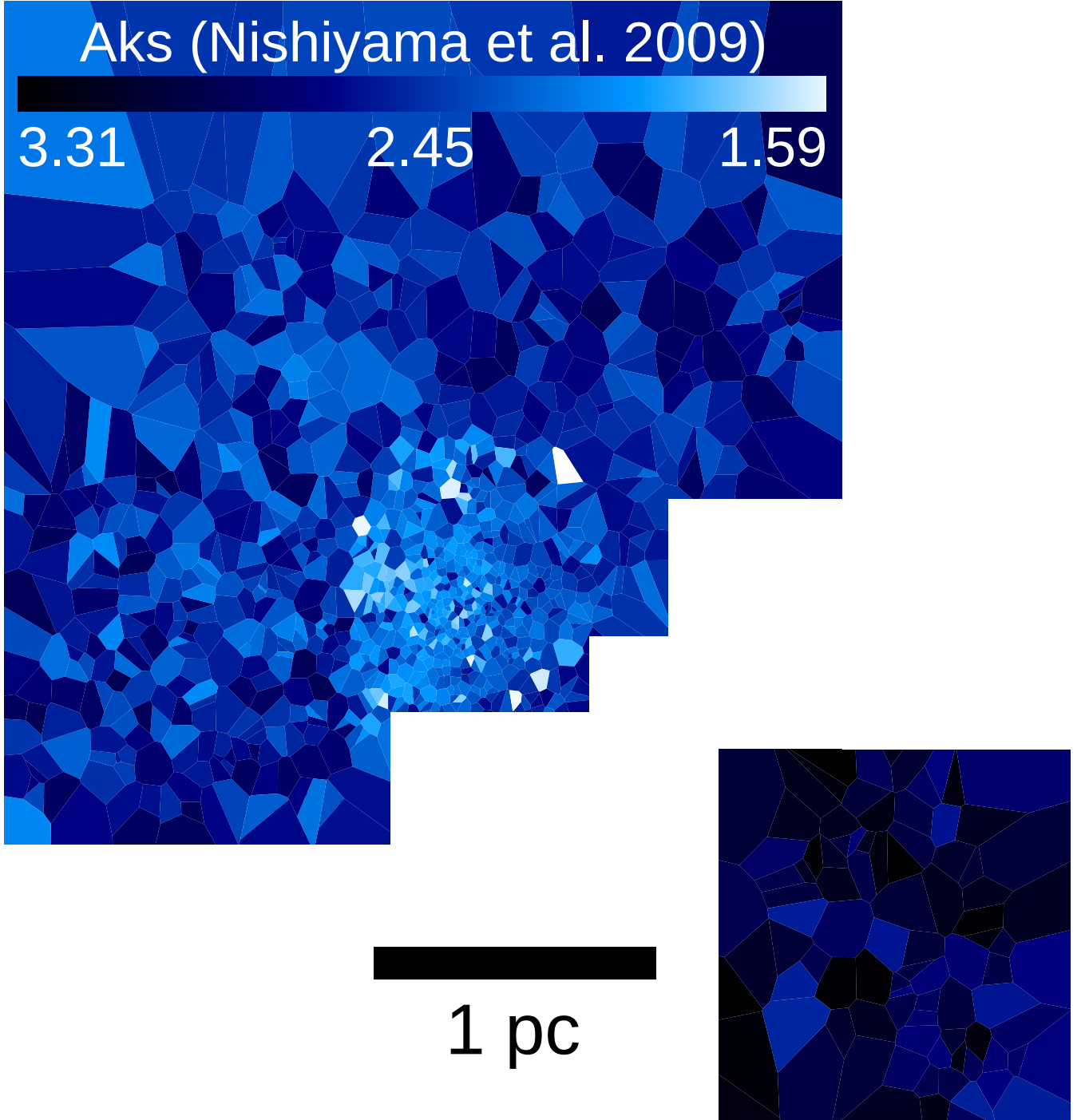


Fig. 10. The extinction map of the Arches cluster using Voronoi diagrams: each star is associated with one and only one cell the color of which is determined by the measured extinction value at the star. A region of lower extinction is present in the center of the cluster while stripes of larger extinction are present in the south west and partly north west of the cluster. The extinction is high and vary up to ~ 2 mag across the cluster. The extinction values derived based on the Rieke & Lebofsky extinction law (1985) vary between $2.1 < A_{K_s} < 4.4$ mag while utilizing the Nishiyama et al. (2009) extinction law yields an extinction range of $1.6 < A_{K_s} < 3.3$ mag. The structure of the two extinction maps based on the two different extinction laws is only marginally different. North is up and East is to the left.

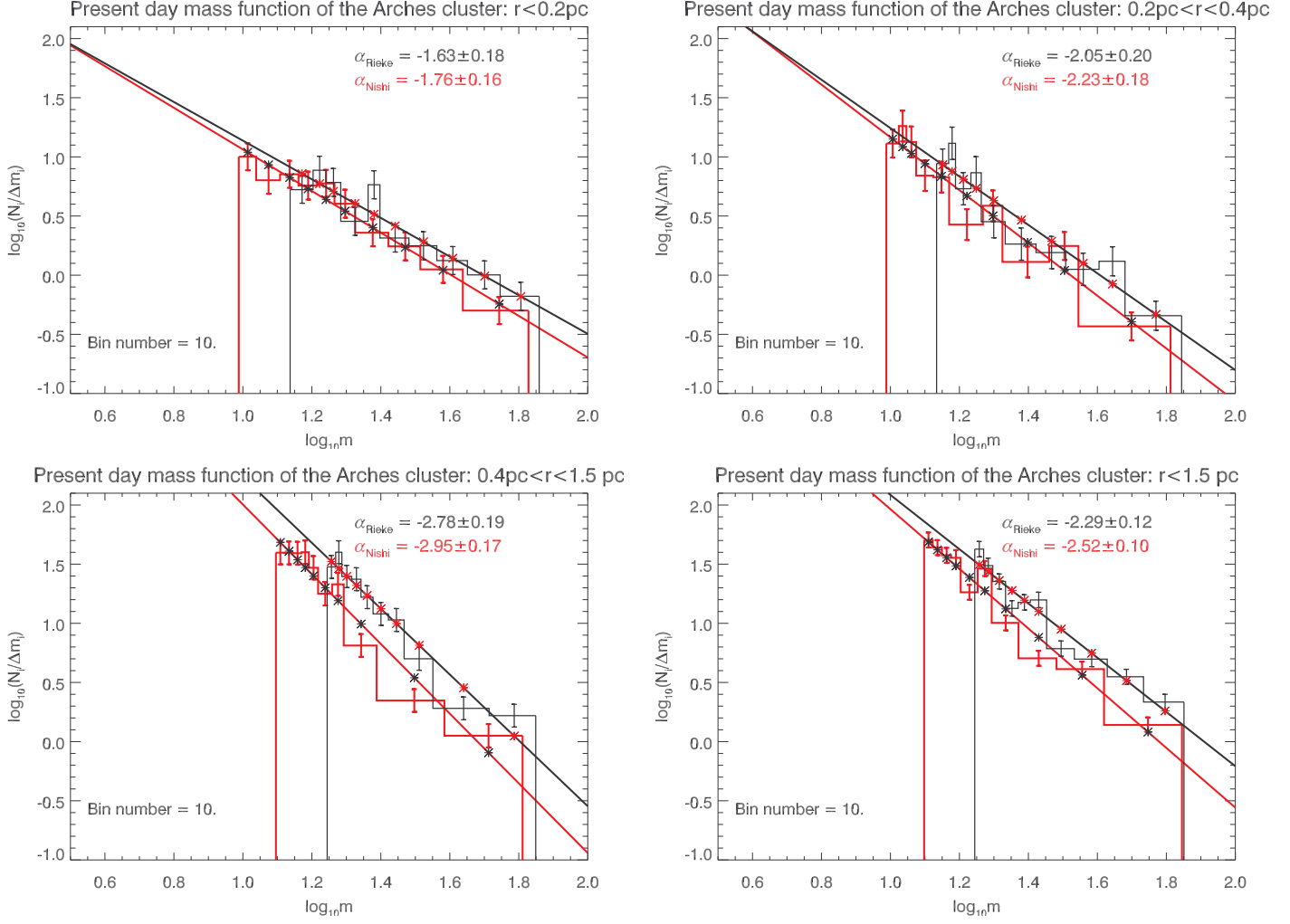


Fig. 11. The present-day mass function of the Arches cluster. Red lines correspond to the mass distribution derived based on the N-EL while black lines represent the mass function assuming the RL-EL. Both mass functions are fitted with a power-law like function with reported slopes of α shown in the respective color. The present-day mass functions are plotted in three regions: (a) the inner core of $r < 0.2$ pc, (b) the intermediate annulus of $0.2 < r < 0.4$ pc and, (c) the cluster outskirts of $0.4 < r < 1.5$ pc. The present-day mass function steepens as we move outward from the cluster center. The complete present-day mass distribution of the cluster within $r < 1.5$ pc (d) which is consistent within the uncertainties with a Salpeter IMF. The illustrated error for the slopes just represent the numerical fitting uncertainties.

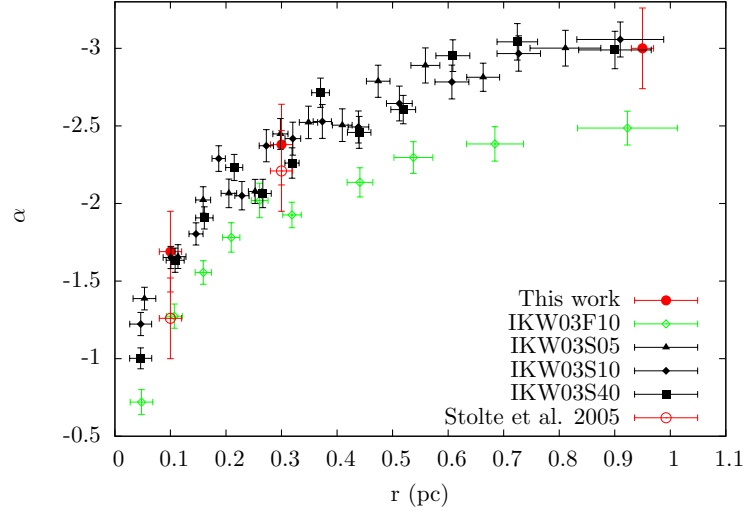


Fig. 12. The figure is adopted from Harfst et al. (2010) their Fig. 13, and compares the mass function slopes from the best fitting models of N-body simulations of the Arches cluster to the observed values of this work and also from Stolte et al. (2005). The black filled symbols represent the models with Salpeter IMF with different lower mass limits while green open symbols correspond to a model with flat IMF. The three Salpeter and the one flat IMF models deviate primarily at larger radii ($r > 0.4$ pc). The derived slope from a model starting with a Salpeter IMF at birth in the radius of 1 pc is $\alpha \sim -3$ which is in good agreement with our finding of $\alpha_{Nishi} \sim -2.95 \pm 0.26$ in the outskirts of the Arches cluster.